Nuclear Science and Techniques (2026) 37:3
https://doi.org/10.1007/s41365-025-01857-3

Conceptual design and preliminary feasibility study of fluid-driven suspended control rods for molten salt reactors

Jin-Tong Cao[1,2] · Gui-Feng Zhu[1,2] · Chang-Qing Yu[1] · Ya-Fen Liu[1,2] · Yang Zou[1,2] · Rui Yan[1,2] · Hong-Jie Xu[1,2]

Received: 1 April 2025 / Revised: 14 May 2025 / Accepted: 18 May 2025 / Published online: 5 December 2025

Abstract

Molten salt reactors, being the only reactor type among Generation IV advanced nuclear reactors that utilize liquid fuels, offer inherent safety, high-temperature, and low-pressure operation, as well as the capability for online fuel reprocessing. However, the fuel-salt flow results in the decay of delayed neutron precursors (DNPs) outside the core, causing fluctuations in the effective delayed neutron fraction and consequently impacting the reactor reactivity. Particularly in accident scenarios—such as a combined pump shutdown and the inability to rapidly scram the reactor—the sole reliance on negative temperature feedback may cause a significant increase in core temperature, posing a threat to reactor safety. To address these problems, this paper introduces an innovative design for a passive fluid-driven suspended control rod (SCR) to dynamically compensate for reactivity fluctuations caused by DNPs flowing with the fuel. The control rod operates passively by leveraging the combined effects of gravity, buoyancy, and fluid dynamic forces, thereby eliminating the need for an external drive mechanism and enabling direct integration within the active region of the core. Using a 150 MWt thorium-based molten salt reactor as the reference design, we develop a mathematical model to systematically analyze the effects of key parameters—including the geometric dimensions and density of the SCR—on its performance. We examine its motion characteristics under different core flow conditions and assess its feasibility for the dynamic compensation of reactivity changes caused by fuel flow. The results of this study demonstrate that the SCR can effectively counteract reactivity fluctuations induced by fuel flow within molten salt reactors. A sensitivity analysis reveals that the SCR's average density exerts a profound impact on its start-up flow threshold, channel flow rate, resistance to fuel density fluctuations, and response characteristics. This underscores the critical need to optimize this parameter. Moreover, by judiciously selecting the SCR's length, number of deployed units, and the placement we can achieve the necessary reactivity control while maintaining a favorable balance between neutron economy and heat transfer performance. Ultimately, this paper provides an innovative solution for the passive reactivity control in molten salt reactors, offering significant potential for practical engineering applications.

Keywords Molten salt reactor · DNP flow-induced reactivity · Passive control · Suspended control rod

1 Introduction

Among the six Generation IV advanced reactor designs, molten salt reactors (MSRs) uniquely use liquid fuel. The molten salt used serves as both the fuel and coolant circulating within a single primary loop. This design ensures inherent safety, enables high-temperature and low-pressure operation, supports online fuel reprocessing, and is ideally suited for thorium fuel [1–3]. The inherent properties of the liquid fuel offer specific advantages for reactivity control, including the capacity for online refueling and reprocessing, which aids in maintaining a low level of backup reactivity

This work was supported by Youth Innovation Promotion Association of Chinese Academy of Sciences (No. 2020261), Strategic Priority Research Program of Chinese Academy of Sciences (No. XDA02010000), and the Young Potential Program of Shanghai Institute of Applied Physics, Chinese Academy of Sciences (No. SINAP-YXJH-202412).

✉ Gui-Feng Zhu
zhuguifeng@sinap.ac.cn

[1] State Key Laboratory of Thorium Energy, Shanghai Institute of Applied Physics, Chinese Academy of Sciences, Shanghai 201800, China

[2] University of Chinese Academy of Sciences, Beijing 100049, China

and reducing the demand for reactivity management [4]. However, the use of liquid fuel introduces challenges for reactivity control in MSRs. During the operation, as delayed neutron precursors (DNPs) circulate with the molten salt in the primary loop, a fraction of the delayed neutrons is lost outside the core [5]. The high-velocity fuel-salt flow significantly diminishes the effective fraction of delayed neutrons within the core. Conversely, when the primary loop flow decreases sharply, the delayed neutron precursors are retained within the core, resulting in a pronounced positive reactivity insertion. If the control rod system fails to respond in a timely manner, the reactor would have to depend exclusively on its negative temperature reactivity coefficient for power modulation. However, under these circumstances, the inadequate removal of decay heat causes a significant increase in the core temperature. Simulation studies have demonstrated that under design-basis accident conditions, such as a complete station blackout combined with the inability to quickly scram the reactor, the outlet temperature of a large MSR may increase by 50−100 °C above the normal operating levels [6–8]. Such temperature fluctuations can impose severe thermal shock on the structural materials of the reactor. This poses daunting challenges for the long-term safety and maintenance of MSRs. Consequently, the development of a passive reactivity control device capable of effectively compensating for reactivity fluctuations induced by fuel flow has engineering importance.

Passive safety systems have emerged as fundamental components of modern nuclear reactor designs [9, 10]. By harnessing natural physical laws such as gravity and natural convection, these systems automatically maintain reactor safety and stability during both internal and external accident scenarios without relying on external power or human intervention [11, 12]. Passive reactivity control devices can be classified into two types depending on their driving mechanism. The first type is the flow-driven device, which utilizes variations in coolant flow to trigger the control of rod movement and adjust reactivity, effectively mitigating the incidences of coolant flow and coolant loss. A representative example is the hydraulic suspension passive shutdown assembly (HSPSA), which has been implemented in Russia's BN series sodium-cooled fast reactors, as well as in China's demonstration fast reactor, CFR-600. HSPSA represents a critical technology for advanced nuclear reactor systems. Initially developed by Russia's Institute of Physics and Power Engineering (IPPE) and successfully implemented in Russia's BN series sodium-cooled fast reactors (e.g., BN-600 and BN-800), this technology has demonstrated high reliability through extensive theoretical analysis and experimental validations [13, 14]. Recognizing its potential to address China's strategic demand for fast reactor development, Chinese scholars, including Hu Wenjun, prioritized HSPSA as a key technology for domestic research [15, 16]. Building on this foundation, research groups from Xi'an Jiaotong University [17, 18], China Institute of Atomic Energy [19–22], Shanghai Jiaotong University [23–27], and Xi'an University of Technology [28–34] have systematically explored the hydraulic characteristics, dynamic behavior, rod-drop mechanisms, and stability of liquid-suspended passive shutdown assemblies through theoretical analysis, numerical simulation, and experimental verification. These offered critical theoretical support and technical guidance for optimizing HSPSA design. Notably, the Chinese research teams have advanced the technology by addressing key challenges under complex operating conditions. Their work has contributed to the successful implementation of HSPSA in China's CFR-600 demonstration fast reactor and global technological progress. The second category is temperature-driven devices, which regulate reactivity based on variations in the coolant temperature and are effective at mitigating overpower accidents and loss-of-heat-removal scenarios. Representative applications include the buoyancy driven shutdown rod (BDSR) in the advanced fluoride-cooled, high-temperature pebble-bed reactor use in the USA and the floating absorber for safety at transient (FAST) utilized in South Korea's advanced sodium-cooled fast reactors [35, 36]. A research team at the University of New Mexico systematically investigated the fluid dynamic properties, thermal response characteristics, and system coupling behavior of BDSR by developing theoretical models. They performed numerical simulations and experimental validation [35, 37]. Researchers at the Korea Advanced Institute of Science and Technology (KAIST), utilizing their developed transient analysis model, have extensively examined the response characteristics of FAST under various design-basis accident conditions [38–40]. Through design optimization, they effectively mitigated power and temperature oscillations under particular scenarios, thereby markedly improving the overall safety of sodium-cooled fast reactors [41–43].

In summary, significant progress has been made in developing passive safety systems, with particularly notable advancements in flow-driven and temperature-driven reactivity control devices. The distinctive liquid fuel operation of MSRs introduces novel technical challenges, with reactivity fluctuations induced by the fuel flow being particularly significant. Because the reactivity fluctuations induced by fuel flow exhibit marked flow-dependence and immediate response characteristics, whereas fuel temperature variations are relatively gradual—rendering temperature-based compensation mechanisms inherently lagging—flow-driven devices are more appropriate for compensating for the reactivity fluctuations in MSRs. Therefore, drawing on previous research and design experience with flow-driven devices, this paper proposes an innovative passive fluid-driven suspended control rod design. The control rod is predominantly driven by gravity, buoyancy, and fluid dynamic forces. Under

rated core flow conditions, the fluid thrust suspends the rod at its upper limit position, thereby minimizing the neutron absorption. In contrast, during a sudden decrease in the core flow, the rod falls under gravity, thereby introducing a negative reactivity to counterbalance the positive reactivity perturbations resulting from the reduced flow. In this paper, a 150 MWt thorium-based MSR is used as the reference design. A mathematical model is developed to systematically analyze the effects of key parameters—such as geometric dimensions and material density—on the performance of the suspended control rod. The model is used to compute the motion characteristics of the rod under various core flow conditions and evaluate the feasibility of compensating for reactivity fluctuations induced by the fuel flow.

The remainder of this paper is organized into four main sections: Section 2 thoroughly describes the structural features and key design parameters of the core model while providing a detailed analysis of the operating principles and structural design of the fluid-driven control rod. Section 3 focuses on computational methods, including the determination of reactivity insertion at various rod positions, the methodology for establishing rod positions under diverse core flow conditions, and optimization strategies for the design parameters. Section 4 analyzes and discusses the results, with a focus on (1) quantifying the relationship between the flow-induced reactivity changes and core flow; (2) conducting a parameter sensitivity study of the correlation between rod position and core flow; (3) analyzing the control rod's resistance to interference from density variations; (4) identifying the key factors affecting the reactivity worth of the control rod; and (5) assessing the performance of the fluid-driven suspended control rod in compensating for the flow-induced reactivity fluctuations. Section 5 concludes the study by summarizing the key findings and innovations and outlining potential directions for future research.

2 Introduction of core model and fluid-driven control rods

This section provides an overview of the core model configuration, design principles, and operational mechanisms of the fluid-driven control rod system. The discussion begins with a detailed description of the core architecture and critical design parameters of the reference 150 MWt thorium-fueled MSR. Subsequently, the two primary variants of the fluid-driven control rods are examined—namely, floating control rod (FCR) and suspended control rod (SCR)—with explanations of their structural configurations and operational principles. Through a comparative analysis of the characteristics of FCR and SCR, this section establishes the superior suitability of the SCR for mitigating flow-induced reactivity perturbations in MSR systems.

2.1 Core model

The core model adopted in this paper is a liquid-thorium-based MSR with a thermal neutron spectrum and rated thermal power of 150 MWt [44]. The fuel salt comprises a fluoride-lithium-beryllium eutectic containing thorium and enriched uranium; its thermophysical parameters are provided in Table 1. Graphite serves as the moderator. The reactor comprises essential components such as the core active region, control rod assembly, graphite reflector, upper and lower plenums, downcomer annulus, internal support structures, and primary reactor vessel (Fig. 1). The core configuration features a hexagonal close-packed arrangement with an equivalent diameter of 3.0 m and active region height of 3.2 m, consisting of 241 uniformly distributed hexagonal graphite blocks, each with a side length of 18 cm. Each graphite block contains a central flow channel with a diameter of 6 cm, forming the primary path for fuel-salt circulation. The graphite array is encased in a graphite reflector 20 cm thick. The core barrel encloses the reflector assembly, whereas the downcomer annulus is formed between the core barrel and primary reactor vessel, which houses the entire reactor structure. The core's principal design parameters are summarized in Table 1.

Six control rod guide tubes are symmetrically located at the fourth radial ring of the graphite assemblies (denoted by "#" in Fig. 1), ensuring physical isolation between the fuel salt and control rod assemblies while facilitating the vertical movement of the control rods with complete separation from the fuel salt. The control rod system comprises six individual rods, each serving a specific function. These rods are actuated using electric drive mechanisms, which facilitate precise positioning via electrical signal control. In pump coast-down scenarios, the emergency shutdown system is automatically activated when the core flow rates fall below predefined safety thresholds. However, reliance on electrical

Table 1 Fuel-salt properties (T is temperature in °C)

Parameters	Values
Power (MWt)	150
Reactor vessel size (m^2)	3.54×3.6
Inlet and outlet temperature (°C)	600–700
Primary loop fuel flow (kg/s)	1000
Moderator	Graphite
Fuel composition	LiF-BeF_2-ThF_4-UF_4
U-235 enrichment	19.75%
Fuel thermal expansion coefficient (Δ V/V/K)	1.7×10^{-4}
Fuel density (kg/m^3)	$3009.80 - 0.4608T$
Fuel viscosity (Pa s)	$2.524 \times 10^{-7}T + 1.378 \times 10^{-4}T + 0.1317$

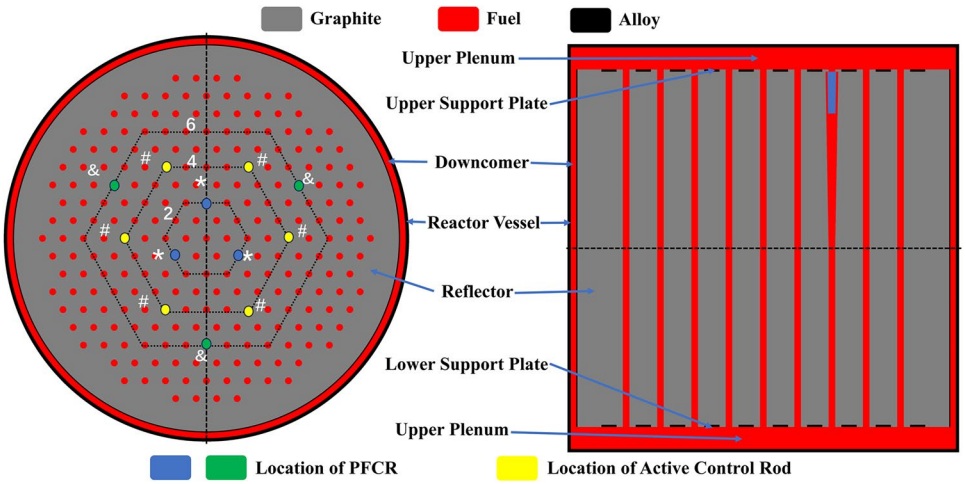

Fig. 1 (Color online) Cross (left) and longitudinal (right) section diagrams of the core

signal transmission in the control rod actuation mechanism introduces potential failure modes, including signal loss during station blackout conditions or mechanical seizures of the control rods despite valid signals. Such failure mechanisms can compromise the capacity of the reactor to execute emergency shutdown after a pump failure [45].

Building on the preceding analysis, this paper introduces an innovative passive fluid-driven control rod (PFCR) design concept, specifically developed to mitigate the reactivity insertion risks during anticipated transient-without-scram scenarios in pump coast-down events. The PFCR system incorporates a flexible core deployment strategy based on the reactivity compensation requirements. For minimal interference with the active control system, PFCR units are positioned at the midpoints of the hexagonal ring segments (with active control rods located at the vertices of the hexagonal rings), as indicated by the "*" and " &" markers in Fig. 1. The deployment strategy for PFCR units is determined by specific reactivity control requirements. In scenarios with lower reactivity control demands, PFCR units are positioned radially outward from the core centerline with minimal population density, as exemplified by a single PFCR installation at the sixth radial ring position (indicated by one of the green " &" markers in Fig. 1). Conversely, for enhanced reactivity control requirements, PFCR units are positioned closer to the core centerline with an increased population density, as demonstrated by the installation of three PFCR units at the second radial ring position (denoted by blue "*" markers in Fig. 1).

2.2 Structure and working principles of fluid-driven control rods

The primary objective of the PFCR system is to compensate for the insertion of positive reactivity following a reduction in the core flow, thereby effectively preventing temperature excursions during pump seizure events. Based on the distinct operational principles, PFCR systems are categorized into two main types: FCR and SCR.

The FCR features a cylindrical configuration that comprises essential components—namely, a cladding, neutron absorber, weighting module, and gas plenum—vertically integrated into the molten salt circulation channel. The cladding isolates the molten salt, whereas the neutron absorber captures thermal neutrons. The weighting module facilitates precise density and center-of-gravity adjustments, whereas the gas plenum performs the dual functions of density modulation and fission gas containment. The material specifications include a nickel-based alloy (density: 8900 kg/m^3) for the weighting module, Gd_2O_3 (density: 5870 kg/m^3) for the neutron absorber, and helium gas (density: 0.17 kg/m^3) in the plenum chamber. Precise density control is achieved by optimizing the volume ratios between the weighting module and the gas plenum, with the neutron absorber occupying 80% of the total rod length. The detailed FCR configuration is shown in Fig. 2a. The mean density of the FCR is engineered to be lower than that of the molten salt, resulting in partial rod protrusion above the liquid level and a buoyant suspension within the fuel salt. FCR motion is governed by the equilibrium between the gravitational, buoyant, and hydrodynamic forces. Increased core flow enhances hydrodynamic forces, which induce upward rod movement and reduce the buoyancy until a dynamic equilibrium is established, thereby stabilizing the FCR at a specific elevation. Conversely, reduced core flow results in a downward movement toward a new equilibrium position.

As depicted in Fig. 2b, the SCR shares similar components and functions with the FCR but features a truncated conical geometry characterized by a wider upper section and narrower base. Correspondingly, the flow channel is designed as a vertically oriented, upwardly expanding conical graphite conduit. The mean density of the SCR exceeds that of the molten salt, resulting in complete submersion and suspension within the fuel salt. Similar to the FCR, SCR

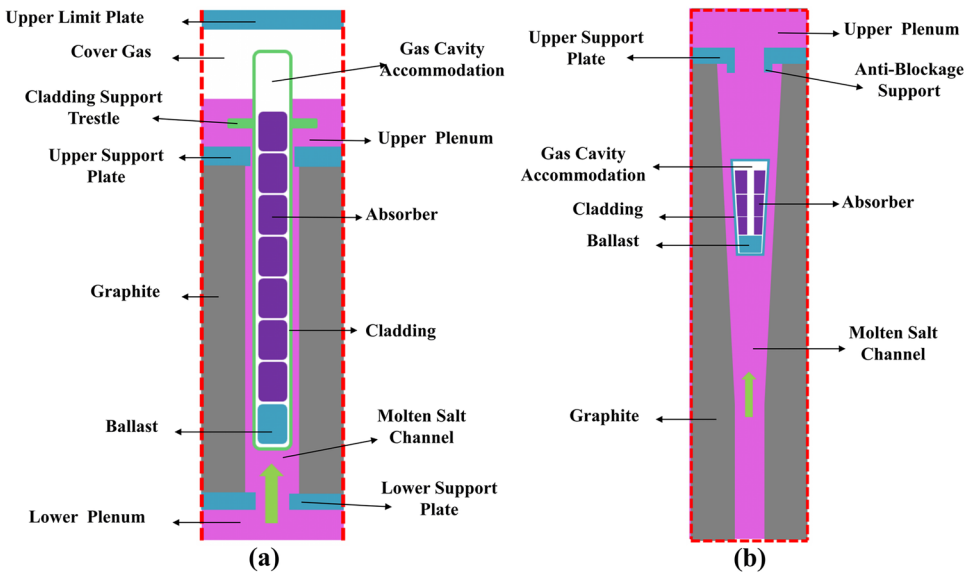

Fig. 2 (Color online) Schematic diagram of the FCR **a** and SCR **b** structures

operation relies on the equilibrium between gravitational, buoyant, and hydrodynamic forces. Fuel-salt circulation through the conical conduit establishes a pressure differential across the upper and lower surfaces of the SCR. This generates hydrodynamic forces. When these hydrodynamic forces exceed the resultant of gravitational and buoyant forces, the upward rod movement commences. The upward SCR movement increases the annular flow area between the rod and conical conduit, thereby reducing the fuel-salt velocity and consequently decreasing the hydrodynamic forces until a new equilibrium position is established at a specific elevation. The SCR position exhibits a positive correlation with the core flow rate: an increased core flow induces upward SCR movement, whereas a decreased flow results in a corresponding downward displacement.

The motion of the FCR is governed by the dynamic equilibrium between the buoyancy and hydrodynamic forces. As the FCR ascends, the volume of the rod exposed above the liquid surface increases, which in turn reduces its buoyancy. This reduction in buoyancy necessitates greater hydrodynamic forces to preserve the equilibrium, thereby requiring a significant force for effective FCR actuation. Furthermore, heightened hydrodynamic forces generate larger pressure differentials across the FCR, which reduces the flow allocation within its channel. This effect may potentially cause flow obstruction, thereby severely compromising the thermal–hydraulic performance of the channel.

In contrast, the SCR remains fully submerged in the molten salt, maintaining consistent gravitational, buoyant, and hydrodynamic forces. The magnitude of the hydrodynamic force can be regulated precisely by optimizing the differential between the gravitational and buoyant forces. Consequently, the SCR can be actuated with lower hydrodynamic forces, thereby minimizing its impact on the flow distribution in the channel. Moreover, the displacement of the SCR is determined by the height-dependent variation in the surrounding annular flow area. This characteristic enables the precise calibration of the relationship between the rod position and flow rate via optimization of the SCR channel geometry, thereby facilitating an effective compensation for flow-induced reactivity perturbations. The inherent design characteristics of the SCR render it particularly well-suited for mitigating flow-induced reactivity oscillations, thereby demonstrating its superior engineering applicability.

Under static fuel-salt conditions, the SCR maintains a stable equilibrium at the base of the conical conduit because its mean density exceeds that of the molten salt. During fuel-salt circulation, increased core flow rates exacerbate DNP loss, consequently reducing the core reactivity. Concurrently, elevated core flow rates induce the upward movement of the SCR, releasing sufficient reactivity to compensate for the reduction in reactivity induced by DNP loss. Under nominal core flow conditions, the SCR reaches equilibrium at its maximum elevation, with the released reactivity exactly offsetting the reactivity deficit caused by DNP loss. In the pump coast-down scenarios, when fuel-salt circulation terminates, the SCR descends to the base of the conical conduit, introducing a negative reactivity that precisely neutralizes the positive reactivity resulting from DNP accumulation in the core. Throughout its operational trajectory, the SCR remains within the active region of the core. Under normal operating conditions, the SCR is positioned at the top of the active region of the reactor core. As shown in Fig. 3, the fast neutron flux (0.05–20 MeV) at the SCR location is approximately four times lower than that at the core center. Therefore, the neutron-absorbing material is expected to have significantly longer irradiation lifetime. In addition, the SCR does not bear mechanical loads, irradiation does

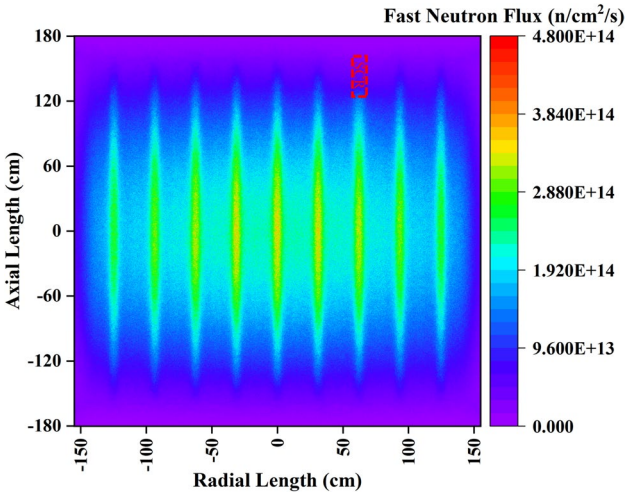

Fig. 3 (Color online) Distribution of fast neutron flux (0.05–20 MeV)

not generate gases, and no internal pressure exists, resulting in minimal overall stress. Therefore, its service life should be comparable to that of the structural materials of the reactor, such as the upper support plate.

The SCR is characterized by a straightforward structural design that does not require complex external drive mechanisms or electrical systems. Consequently, its manufacturing cost is significantly lower than that of conventional electrically driven control rod systems, which often relies on high-reliability motors, signal transmission networks, and multiple redundant components. Furthermore, the SCR employs materials that are resistant to high temperatures, irradiation, and molten salt corrosion and adopts a fully mechanical structure without the requirement for precision components. This design enables reliable long-term operation of MSRs under extreme conditions, thereby significantly reducing the maintenance demands and extending the inspection intervals. As a fully passive system, the SCR can automatically insert control rods under extreme accident scenarios. such as complete power failure or signal loss. This significantly enhances the inherent safety of the reactor core, mitigates the risks of unplanned shutdowns, equipment damage, and personnel hazards, and indirectly reduces long-term operational and insurance expenses.

Existing MSR control rod systems isolate the control rods from the molten salt by installing thin-walled alloy sleeves in the active core region. This avoids radioactive sealing and isolation challenges for the drive mechanisms. This solution was implemented in the US MSRE [46] and China's 2 MW TMSR-LF1 [47] reactors. However, for large-scale MSRs, this approach faces the risk of alloy sleeves experiencing helium embrittlement and rupturing under high-neutron-flux irradiation. This could result in the failure of the primary circuit boundary. In contrast, the SCR is in direct contact with the molten salt and does not require any drive mechanism. This effectively eliminates concerns related to alloy sleeve rupturing and radioactive isolation from the drive system. Moreover, the SCR is fully integrated within the active core region, thereby preventing control rod ejection accidents.

In summary, the SCR system offers not only outstanding economic advantages and reduced manufacturing and maintenance costs but also improved safety, which further supports a reduction in long-term operational and insurance expenditures.

3 Reactivity computation and SCR dynamic equilibrium modeling

This section delineates the methodological framework employed for computing the reactivity and modeling the dynamic equilibrium of the SCR. The computational framework begins with an OpenMC-based evaluation of SCR reactivity variations across multiple insertion depths and diverse design configurations. Subsequently, the reactivity perturbations induced by the fuel flow are quantified using a point kinetics reactor model. A comprehensive dynamic equilibrium model for the SCR is developed by incorporating a detailed force analysis under a range of core flow conditions. The relationship between the equilibrium position and flow rate is established by integrating the motion equations with pressure drop computations. The methodological framework culminates in an optimization algorithm that employs iterative computations to determine SCR channel flow characteristics and equilibrium positions while simultaneously identifying the optimal parameters satisfying the reactivity control specifications.

3.1 SCR reactivity worth calculation

The neutronics calculations in this study were performed using OpenMC code. Because its development by the Computational Reactor Physics Group at the Massachusetts Institute of Technology in 2011, OpenMC has benefited from continuous enhancements and significant contributions from the open-source community. OpenMC is a Monte Carlo neutron transport code that provides essential capabilities, including fixed-source calculations, effective multiplication factor determination, and subcritical system analysis. The program features an extensive Python API that facilitates functionalities, such as input file generation, data post-processing, and result visualization [48].

Leveraging OpenMC, we developed a comprehensive computational core model to evaluate the effective multiplication factor (k_{eff}) of the SCR at various insertion depths under different design parameters—including geometric configurations, density, and deployment strategies. The core

reactivity (ρ) was computed using Eq. (1), whereas SCR reactivity changes ($\Delta\rho$) at various positions were determined using Eq. (2). Subsequently, the resulting data were processed using polynomial fitting to generate the SCR position-reactivity worth curve.

$$\rho = \frac{k_{\text{eff}} - 1}{k_{\text{eff}}}, \tag{1}$$

$$\Delta\rho = \rho(h) - \rho(h_0), \tag{2}$$

where $\rho(h)$ is the reactivity of the SCR at position height h, and $\rho(h_0)$ is the reactivity of the SCR at the initial position.

3.2 DNP flow-induced reactivity

During MSR operation, fuel-salt circulation induces fluctuations in the effective delayed neutron fraction, which results in core reactivity oscillations. Accurately determining these flow-induced reactivity changes theoretically requires coupling the neutron transport with fluid dynamics simulations—a level of complexity that exceeds the scope of this study. Comprehensive methodologies for addressing this issue are detailed in Ref. [49]. In this investigation, a point kinetics model that neglects spatial effects is employed to approximate fuel flow-induced reactivity changes ($\Delta\rho_{\text{fluid}}$) [50], with the associated estimation formulation expressed as

$$\Delta\rho_{\text{fluid}} = \beta - \sum_{i=1}^{6} \frac{\beta_i \lambda_i}{\lambda_i + (1 - e^{-\lambda_i \tau_{\text{el}}})/\tau_{\text{c}}}. \tag{3}$$

Among these parameters, β represents the effective delayed neutron fraction in the absence of fuel-salt flow in the core, β_i denotes the fraction of delayed neutrons in each group, λ_i is the decay constant for each group of DNP, τ_{c} indicates the residence time of the fuel salt in the core, and τ_{el} represents the residence time of the fuel salt outside the core. The parameters τ_{c} and τ_{el} are closely related to the core flow rate: As the core flow rate increases, τ_{c} decreases, whereas τ_{el} increases. With a further increase in the core flow rate, the fuel salt is recycled back into the core, causing the rates of change of τ_{c} and τ_{el} to decrease until they eventually stabilize. The fractions and decay constants for each group of delayed neutrons are listed in Table 2 [44].

3.3 SCR dynamic equilibrium modeling

The movement of the SCR is dictated by the interplay between gravitational, buoyant, and hydrodynamic forces, with its equilibrium position under varying core flow conditions as determined by their dynamic balance. Figure 4 presents a schematic of the force balance analysis for the SCR.

Based on the force analysis, the corresponding motion equation for the SCR is derived as follows:

$$M_{\text{s}} \frac{\mathrm{d}^2 h}{\mathrm{d}t^2} = F_{\text{d}} + F_{\text{b}} - G, \tag{4}$$

where M_{s} represents the mass of the SCR, h is the height of the SCR's top from the bottom of the conical pipeline, and t represents the time. G, F_{b}, and F_{d} denote the gravitational, buoyancy, and fluid dynamic forces acting on the SCR, respectively. These forces are calculated using the following relationships:

$$\begin{aligned} G &= \rho_{\text{s}} V_{\text{s}} g, \\ F_{\text{b}} &= \rho_{\text{f}} V_{\text{s}} g, \\ F_{\text{d}} &= \Delta p_{\text{s}} A_{\text{s}}, \end{aligned} \tag{5}$$

$$V_{\text{s}} = \pi \left[\frac{1}{4} D_{\text{s}}^2 L_{\text{s}} + \frac{1}{6} D_{\text{s}} L_{\text{s}}^2 \tan\theta + \frac{1}{3} L_{\text{s}}^3 \tan^2\theta \right]. \tag{6}$$

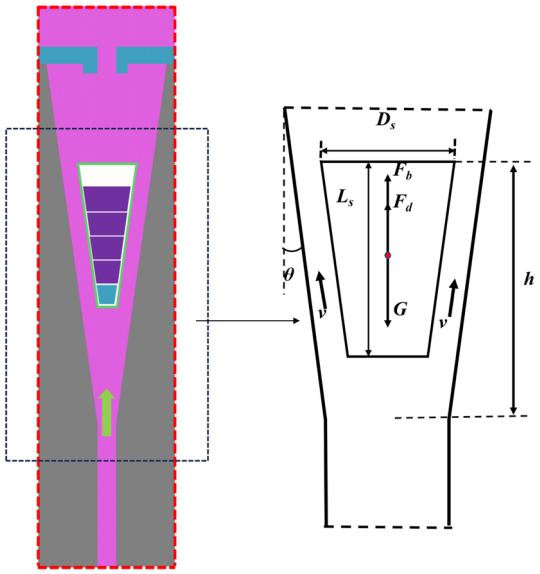

Fig. 4 (Color online) SCR force analysis

Table 2 Fraction and decay constant of each group of delayed neutrons

Group	1	2	3	4	5	6
β_i (pcm)	15.31	108.11	107.45	307.51	82.93	41.96
λ_i (s)	0.0124	0.0305	0.111	0.301	1.14	3.01

Table 3 Friction loss coefficient at different Reynolds numbers in a circular pipe

Flow regime	Empirical formula
$Re < Re_1$	$\lambda = 64/Re$
$Re_1 \le Re \le Re_2$	$\lambda = \frac{(0.3164/Re_2^{0.25} - 64/Re_1)}{(Re_2 - Re_1)}(Re - Re_1) + \frac{64}{Re_1}$
$Re > Re_2$	$0.3164/Re^{0.25}$

$Re_1 = 1160/\varepsilon^{0.11}$, $Re_2 = 2090/\varepsilon^{0.0635}$

Here, V_s, A_s, L_s, and D_s denote the SCR volume, upper base area, length, and upper base diameter, respectively; θ represents the conical taper angle; ρ_s indicates the SCR mean density; ρ_f signifies the fuel-salt density; and g is the gravitational acceleration. Δp_s denotes the flow-induced pressure differential across the SCR. As the SCR is embedded in the active region of the core—with only minor differences in the cross-sectional areas between its top and bottom—and under the assumption of a uniform core temperature distribution, the lift and acceleration pressure drops are neglected, accounting solely for the friction and local pressure drops. The friction and local pressure drops are computed using the following expressions:

$$\Delta p_\lambda = \frac{1}{2}\lambda \rho_f v_s^2 \frac{L_s}{D_s}, \tag{7}$$

$$\Delta p_\zeta = \frac{1}{2}\zeta \rho_f v_s^2, \tag{8}$$

$$\Delta p_s = \frac{1}{2}\left(\lambda \frac{L_s}{D_s} + \zeta\right)\rho_f v_s^2, \tag{9}$$

where v denotes the mean flow velocity of the fuel salt through the SCR conduit. The parameters λ and ζ represent the friction factor and local loss coefficient, respectively. The friction factor λ is determined using the Reynolds number ($\mathrm{Re} = \rho v D_e/\mu$, where D_e is the equivalent diameter of the pipe, and ρ, v, and μ denote the fluid density, velocity, and viscosity, respectively. As Δp_λ is relatively minor, the influence of fluid viscosity variations on Δp_s is negligible. Consequently, the effect of temperature on the fuel-salt viscosity is disregarded in this paper, and the viscosity of the fuel salt at 650 °C, $\mu = 0.0072895$ Pa·s, is used throughout the analysis.). It is also affected by the relative roughness ε ($\varepsilon = \Delta/D_e$, where Δ, defined as the absolute roughness, represents the average height of the surface asperities; in this study, $\Delta = 10^{-4}$ m). The local loss coefficient ζ is primarily affected by the geometric configuration of the conduit. In practice, the precise theoretical determination of λ and ζ is challenging, necessitating an estimation through experimental measurements or empirical correlations. Computational approaches for determining λ and ζ across various flow regimes are systematically summarized in Tables 3 and 4, respectively [51].

Table 4 Local loss coefficients for different pipe geometries

Pipe geometry	Loss coefficient
Gradually expanding pipe	$\zeta = k_{grad} \times \left(1 - \frac{A_1}{A_2}\right)^2$
Suddenly expanding pipe	$\zeta = \left(1 - \frac{A_1}{A_2}\right)^2$
Suddenly contracting pipe	$\zeta = k_{sudd} \times \left(1 - \frac{A_1}{A_2}\right)^2$

$k_{grad} = 7.19 \times 10^{-4}\alpha^2 + 3.33 \times 10^{-3}\alpha + 0.065$

$k_{sudd} = -0.189\left(\frac{A_1}{A_2}\right)^2 - 0.306\frac{A_1}{A_2} + 0.503$

α is the expansion angle of the diffuser.

A_1 and A_2 are the initial and final cross-sectional areas, respectively

To determine the friction loss coefficient for a section with a noncircular cross-section, we multiply the friction loss coefficient for a circular pipe by the corresponding shape influence factor [52]:

$$\lambda_n = k_n \lambda, \tag{10}$$

where λ represents the friction loss coefficient for circular pipe sections under identical Reynolds numbers, λ_n denotes the friction loss coefficient for the non-circular pipe sections under the same Reynolds number, and k_n is the cross-sectional shape correction coefficient.

For laminar flow, the correction factor for a circular annular tube depends on the ratio of its inner to outer diameters [53]:

$$k_n = \frac{\left(1 - \left(d/D_0\right)\right)^2}{1 + \left(d/D_0\right)^2 + \left(1 - \left(d/D_0\right)\right)^2 \ln\left(d/D_0\right)}. \tag{11}$$

Here, d and D_0 denote the inner and outer diameters, respectively.

For turbulent flow, the friction loss coefficient λ_n for a circular annular tube can be calculated using the following equation [54]:

$$\lambda_n = \left(\frac{0.02d}{D_0 + 0.98}\right)\left(\frac{1}{\lambda} - 0.27\frac{d}{D_0} + 0.01\right). \tag{12}$$

By combining Eqs. (4) and (5), at the steady state (i.e., when $\mathrm{d}^2h/\mathrm{d}t^2 = 0$), the pressure drop acting across the SCR remains constant, that is,

$$\Delta p_{s,stable} = \frac{(\rho_s - \rho_f)V_s g}{A_s}. \tag{13}$$

Furthermore, combining Eqs. (9) and (13) yields

$$v_{\mathrm{s,stable}} = \sqrt{\frac{2(\rho_{\mathrm{s}} - \rho_{\mathrm{f}})V_{\mathrm{s}}g}{(\lambda L_{\mathrm{s}}/D_{\mathrm{s}} + \zeta)A_{\mathrm{s}}\rho_{\mathrm{f}}}}. \tag{14}$$

Equation (14) indicates that when the SCR reaches a steady equilibrium, the average flow velocity of the fuel salt through the SCR, $v_{\mathrm{s,stable}}$, remains essentially constant and independent of its position. Under these circumstances, the inlet SCR channel flow rate, $Q_{\mathrm{s,stable}}$, is given by

$$Q_{\mathrm{s,stable}} = A_{\mathrm{an}} v_{\mathrm{s,stable}} \rho_{\mathrm{f}}. \tag{15}$$

Assuming $v_{\mathrm{s,stable}}$ remains constant, the flow rate through the SCR channel is primarily determined by the annular area, A_{an}, which varies with the SCR position height, h (i.e., $A_{\mathrm{an}} = f(h)$). For a conical conduit, the relationship between A_{an} and h is expressed as

$$A_{\mathrm{an}}(h) = \pi\left[D_{\mathrm{f}} h \tan\theta + h^2 \tan^2\theta + (D_{\mathrm{f}}^2 - D_{\mathrm{s}}^2)/4\right]. \tag{16}$$

Consequently, under steady-state conditions, a definitive relationship exists between the SCR position height and channel flow rate:

$$\begin{aligned} Q_{\mathrm{s,stable}}(h) &= f(h)\rho_{\mathrm{f}} v_{\mathrm{s,stable}} \\ &= \pi\rho_{\mathrm{f}}\left[D_{\mathrm{f}} h \tan\theta + h^2 \tan^2\theta \right. \\ &\quad \left. + (D_{\mathrm{f}}^2 - D_{\mathrm{s}}^2)/4\right] v_{\mathrm{s,stable}}. \end{aligned} \tag{17}$$

This demonstrates that higher instantaneous flow rates through the SCR channel correspond to larger annular areas and, consequently, higher SCR equilibrium positions. Lower flow rates result in smaller annular areas and lower SCR positions. Moreover, the instantaneous flow rate through the SCR channel is intrinsically linked to the core flow distribution characteristics. Flow distribution is evaluated using a closed parallel-channel model based on two assumptions: (1) uniform flow distribution across all fuel channels and (2) frictional pressure drop as the only influencing factor. For a reactor with 241 channels, the average core pressure drop, ΔP_{av}, is equal to the pressure drop across an individual fuel channel, $\Delta P_{\mathrm{f,fuel}}$, and is expressed as

$$\begin{aligned} \Delta P_{\mathrm{av}} &= \Delta P_{\mathrm{f,fuel}} \\ &= \lambda\rho_{\mathrm{f}} \frac{L_{\mathrm{f}}}{2D_{\mathrm{f}}} \times \left(\frac{4Q_{\mathrm{f}}}{241\rho_{\mathrm{f}}\pi D_{\mathrm{f}}^2}\right)^2, \end{aligned} \tag{18}$$

where L_{f} denotes the fuel channel length, D_{f} is the fuel channel diameter, and Q_{f} denotes the core mass flow rate.

The total pressure drop (ΔP_{CR}) across the SCR channel consists of both frictional and local pressure drop components. As shown in Fig. 3, the SCR channel comprises several successive segments from bottom to top: circular pipe, gradual expansion, sudden contraction, annular, sudden expansion, second gradual expansion segment, second sudden contraction, and final circular pipe segments. Accordingly, the overall pressure drop can be expressed as

$$\Delta P_{\mathrm{CR}} = \Delta P_{\mathrm{tube}} + \Delta P_{\mathrm{grad,exp}} + \Delta P_{\mathrm{s}} + \Delta P_{\mathrm{sud,exp}}, \tag{19}$$

where ΔP_{tube}, $\Delta P_{\mathrm{grad,exp}}$, ΔP_{s}, and $\Delta P_{\mathrm{sud,exp}}$ represent the pressure drops across the circular pipe, gradual expansion, SCR, and sudden expansion segments, respectively. The frictional and local pressure drop components for each segment are determined using Eqs. (7) and (8), respectively. By adjusting the SCR channel flow rate such that its pressure drop matches the average pressure drop in the core, we can determine both the channel flow rate and axial pressure drop distribution.

3.4 Optimization methodology

To vary the core flow conditions, we first employ an iterative computational approach to determine both the SCR channel flow rate and equilibrium position height. Subsequently, an iterative optimization process is conducted to identify the parameters that satisfy the reactivity control specifications, with the iterative calculations executed using Python. The detailed iterative computational workflow is shown in Fig. 5.

The computational procedure commences with parameter initialization, followed by an evaluation of the average core pressure drop (ΔP_{av}) and SCR channel pressure drop (ΔP_{CR}) at the current flow rate. Subsequently, the relative error between the pressure drops is computed. If $(|\Delta P_{\mathrm{av}} - \Delta P_{\mathrm{CR}}|)/\Delta P_{\mathrm{av}} < \Delta E_{\mathrm{p}}$, the core flow distribution is assumed to converge, thereby yielding the SCR channel flow rate Q_{s}. Otherwise, Q_{s} is adjusted and the process is iterated. After the flow distribution is computed, the relative error between the SCR pressure drop (Δp_{s}) at the current position height and steady-state SCR pressure drop ($\Delta p_{\mathrm{s,stable}}$) is evaluated. If the condition $(|\Delta p_{\mathrm{s}} - \Delta p_{\mathrm{s,stable}}|)/\Delta p_{\mathrm{s,stable}} < \Delta E_{\mathrm{p}}$ is not satisfied, the SCR position height is adjusted, and the flow distribution computation is repeated. When convergence is achieved, the core flow rate (Q_{f}), Q_{s}, and position height (h) are output. Subsequently, the reactivity worth ($\Delta\rho_{\mathrm{rod}}$) provided by the SCR and flow reactivity loss ($\Delta\rho_{\mathrm{fluid}}$) at the nominal core flow rate are evaluated. If $|\Delta\rho_{\mathrm{rod}} - \Delta\rho_{\mathrm{fluid}}| < 10^{-4}$, then the reactivity, $\rho_{\mathrm{rod}}(h)$, introduced by SCR across varying core flow rates is computed and output, thereby completing the iterative process and obtaining the optimal geometric parameters for the current configuration. Otherwise, the upper base diameter, D_{s}, and the conical taper angle, θ, of the SCR are adjusted, and the flow distribution computation is repeated.

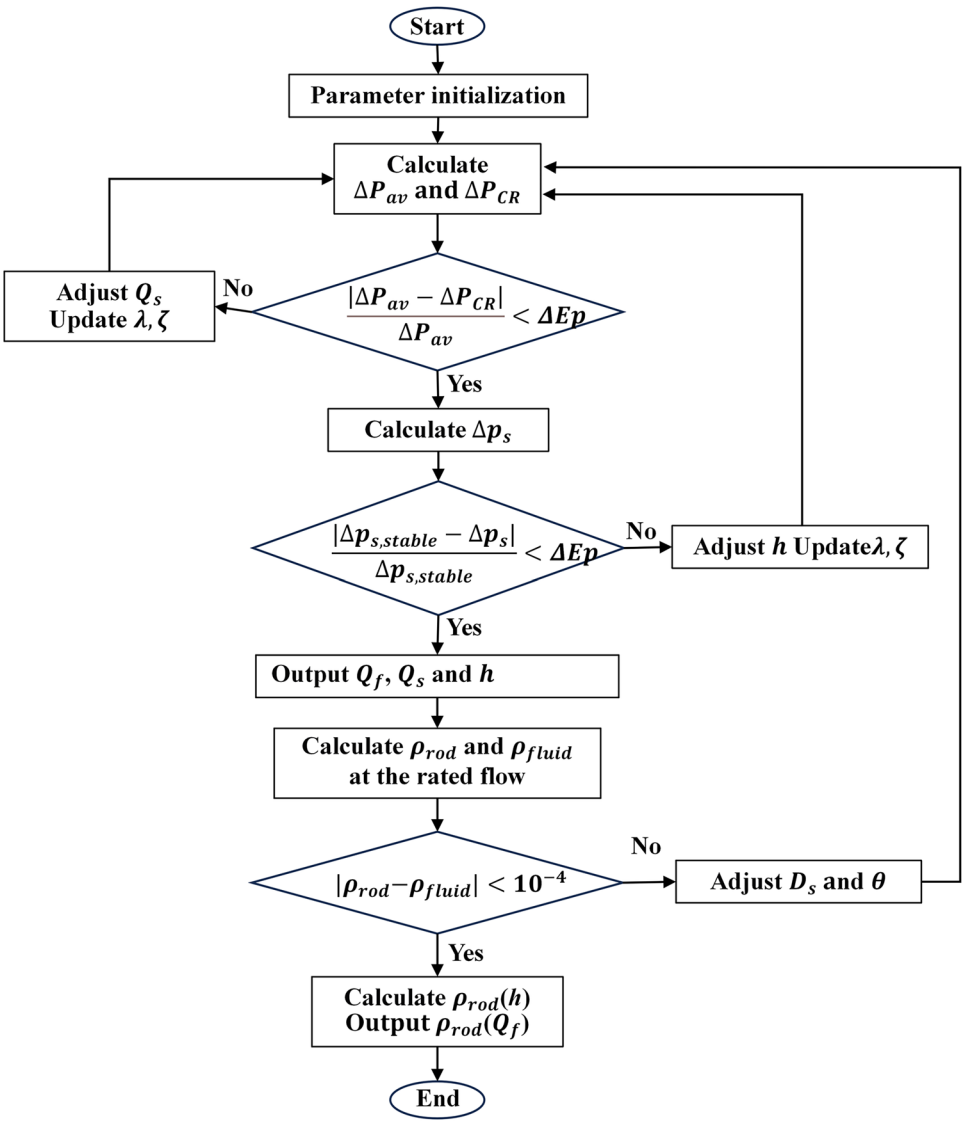

Fig. 5 (Color online) Flowchart of rod position-reactivity calculation for an SCR at different core flows

4 Results and discussion

This section focuses on the performance analysis and discussion of the SCR. First, the relationship between the reactivity changes caused by the fuel flow was examined, elucidating the pattern by which the reactivity loss varies with core flow alterations. Next, we investigated effects of the average density, length, and upper base diameter, and conical taper angle of the SCR on the relationship between its rod positions and the core flow. Subsequently, the discussion addresses the effect of variations in fuel-salt density on the performance of the SCR. Thereafter, the impact of the length, quantity, and position of the SCR on its reactivity worth is analyzed. Finally, we investigated the reactivity compensation capabilities of SCRs using various parameters.

4.1 DNP flow-induced reactivity perturbations

The reduction in the effective delayed neutron fraction caused by DNPs flow is closely related to the residence time of the DNPs both within and outside the core. At lower average fuel flow rates, a reduced proportion of DNP decays outside the core, resulting in a smaller decrease in the effective delayed neutron fraction in the core and, consequently, lower reactivity loss. As the average fuel flow rate increases, the fraction of DNP decaying outside the core increases, causing a greater decrease in the effective delayed neutron fraction within the core and a proportional increase in reactivity loss. When the average fuel flow rate is increased further, DNP recirculates into the active region of the core, resulting in a decrease in the eventual saturation of the fraction of DNP decaying outside the core, at which point the reactivity loss attains its maximum value and then stabilizes.

Figure 6 shows the variations in flow reactivity across different core flow conditions, revealing that at lower core flow rates, the flow reactivity changes considerably with flow variations. At higher flow rates, these changes are notably smaller. Consequently, based on the flow reactivity-core flow variation curve, SCR design should aim for a greater variation in the rod position height or introduce reactivity at lower core flow rates and a smaller variation at higher core flow rates. At the rated core flow, the SCR is expected to release approximately 275 pcm of reactivity.

4.2 SCR position–core flow rate correlation

The correlation between SCR rod position height and core flow directly affects its reactivity insertion characteristics. Thus, a detailed analysis of the key influencing factors is essential for optimizing the SCR structural design and enhancing its performance. As analyzed in Sect. 2.1, this correlation is primarily determined by two key parameters: the SCR stable pressure drop ($\Delta p_{s,stable}$) and flow channel annular area ($A_{an}(h)$). $\Delta p_{s,stable}$ governs the response of the SCR to flow variations and influences the initial start-up flow threshold. As presented in Eq. (13), $\Delta p_{s,stable}$ is a function of the density difference between the SCR and fuel salt, SCR volume, and frontal area. In this context, the SCR volume is determined by the upper base diameter (D_s), conical taper angle (θ), and length (L_s), whereas the frontal area depends solely on D_s. According to Eq. (16), the variation in the flow channel annular area, $A_{an}(h)$, is determined by D_s and θ.

This section uses a controlled variable approach to examine the effect of individual parameters on the SCR position-flow rate relationship. The analysis is conducted using the following initial parameters: $L_s = 30$ cm, $D_s = 7$ cm, $\theta = 2°$, $\rho_s = 2800$ kg/m^3, and $\rho_f = 2710$ kg/m^3. The calculation procedure as shown in Fig. 5 is employed to assess the influence of different parameters on the displacement of the SCR under various core flow rates, as well as the SCR channel flow at the rated core flow rate. The results of these calculations are shown in Figs. 7 and 8.

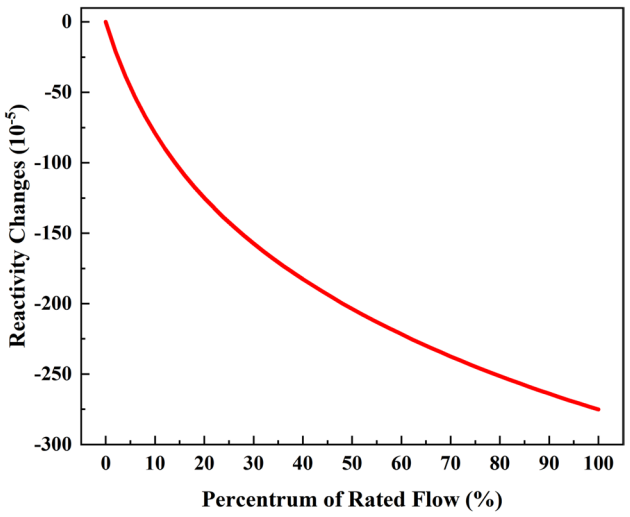

Fig. 6 (Color online) Relationship between DNP flow-induced reactivity changes and core flow rate

The average density (ρ_s) is the most critical parameter that affects SCR motion. As illustrated in Fig. 7a, an increase in ρ_s results in a significant increase in the start-up flow threshold, a rightward shift of the core flow–rod position curve, and a marked decrease in the rod position height at the same core flow rate. Specifically, for every 40 kg/m^3 increase in ρ_s, the start-up flow threshold increases by approximately 10%, whereas the rod position at the rated flow decreases by an average of 10.8 cm. Additionally, the extent of the reduction in the rod position height diminishes as the density increases. Simultaneously, an increase in ρ_s significantly increases the flow resistance within the SCR channel, resulting in a significant decrease in the flow fraction allocated to the SCR. As indicated in Fig. 8a, when ρ_s increases from 2720 to 2880 kg/m^3, the flow fraction decreases from approximately 85% to 53%.

An increase in the SCR length (L_s) similarly increases the start-up flow threshold, shifts the core flow–rod position curve to the right, and reduces the maximum displacement. Specifically, when L_s increases from 20 to 40 cm, the start-up flow threshold increases by 12%, and the rod position at rated flow decreases by 2.4 cm, as illustrated in Fig. 7b. Moreover, a longer L_s increases the frictional resistance within the channel, further diminishing the flow allocated to the SCR. Within the considered range, the SCR channel flow changes by about 6%, as shown in Fig. 8b.

Increasing the upper base diameter (D_s) also results in a higher start-up flow threshold and lower rod position height at the rated flow. However, its effect is minimal and can be neglected, as shown in Fig. 7c. Regarding SCR channel flow, a larger D_s reduces the flow fraction. However, this reduction is limited, as shown in Fig. 8c, indicating a relatively weak effect on the overall SCR performance.

The effect of the conical taper angle (θ) on the SCR rod position–flow relationship is distinct from that of the aforementioned parameters. As θ increases, the start-up flow threshold decreases, whereas the maximum displacement decreases, as shown in Fig. 7d. This occurs because θ influences the SCR volume and determines the annular flow area at various rod positions, which directly affects the correspondence between the rod position and flow rate. An increase in θ can increase the flow fraction in the SCR channel. For example, as θ increases from 1° to 3°, the flow fraction increases from approximately 71–73%, as shown in Fig. 8d. A larger cone angle aids in expanding the annular flow passage area and reduces the local flow resistance,

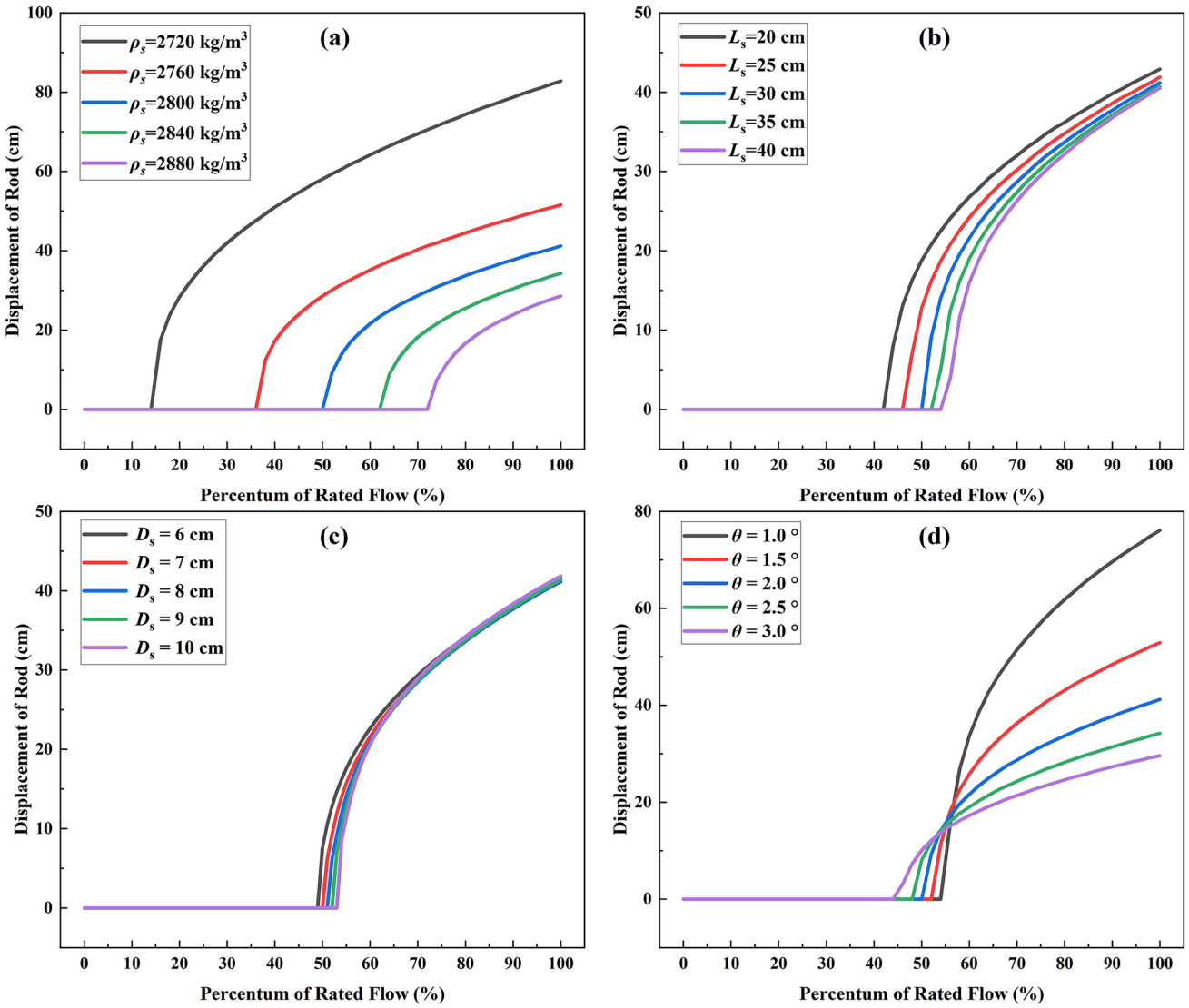

Fig. 7 (Color online) Impact of SCR mean density **a**, length **b**, upper base diameter **c**, and conical taper angle **d** on the SCR position–core flow rate correlation

thereby enhancing channel flow. However, if θ becomes excessively large, it can increase the heat generation rate within the SCR channel, adversely affecting its heat transfer safety.

In summary, the average density exerts the most significant influence on the start-up flow threshold, core flow–rod position relationship, and and channel flow; thus, it is the most critical parameter in SCR structural design. The effects of SCR length and upper base diameter are relatively minor, rendering them secondary control parameters. In contrast, the conical taper angle has a significant impact on the core flow–rod position relationship and may serve as an effective tuning parameter for its optimization. Consequently, the optimization of SCR structural parameters should prioritize controlling the average density, appropriately selecting the SCR length and upper base diameter, and adjusting the conical taper angle to achieve the desired SCR performance for reactivity control.

4.3 Impact of fuel density variations on SCR performance

Variations in the fuel-salt temperature, online fueling, and reprocessing all result in changes in the fuel-salt density. This, in turn, affects the SCR position height at the rated core flow. Assuming a constant SCR average density, a decrease in the fuel-salt density causes a corresponding reduction in the SCR position height. However, if the fuel-salt density exceeds the SCR average density, the SCR remains buoyant at its highest position and does not descend, even in

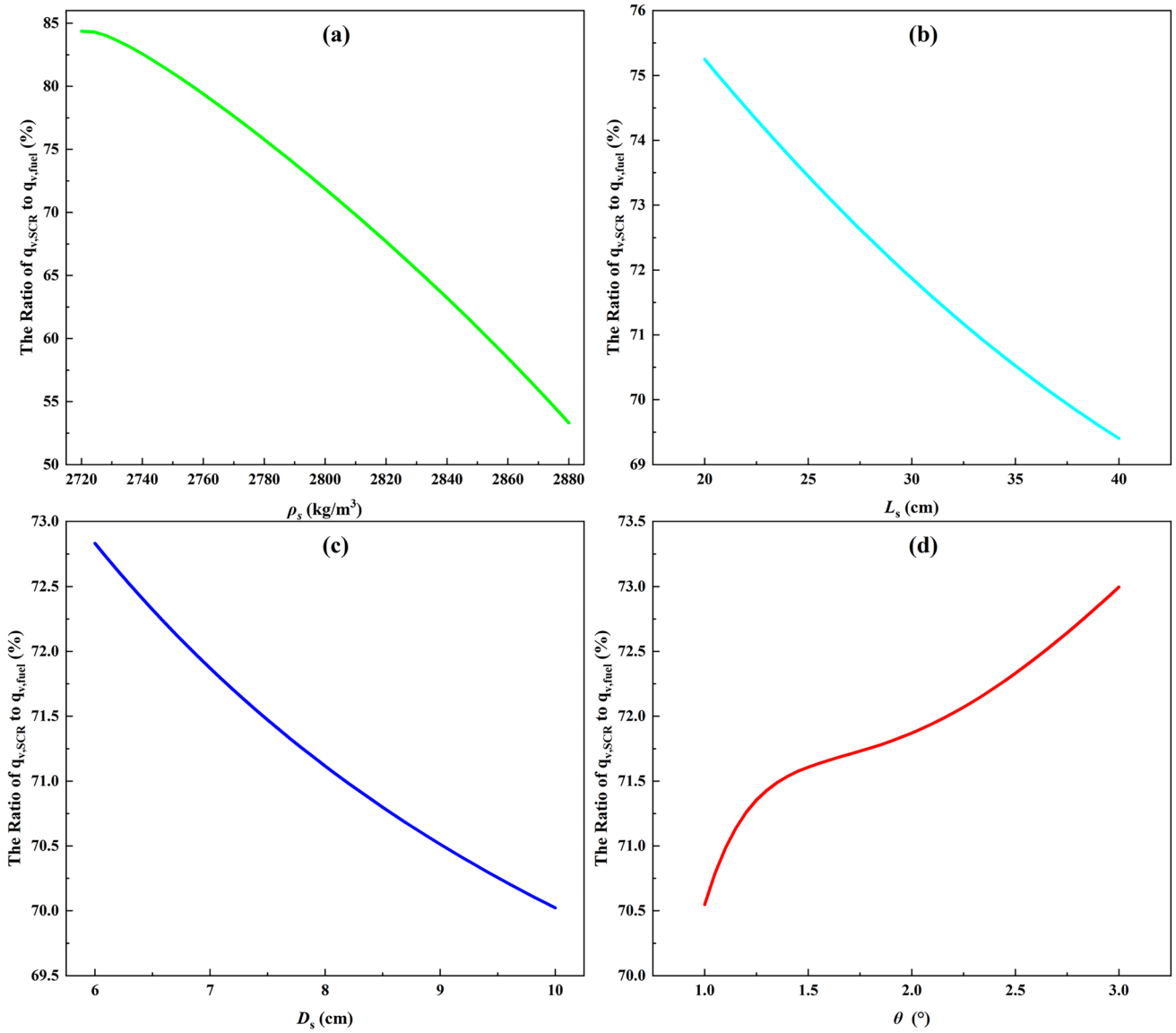

Fig. 8 (Color online) Impact of SCR mean density **a**, length **b**, upper base diameter **c**, and conical taper angle **d** on the SCR channel flow rate

flow-loss scenarios. Therefore, given the dynamic variations in fuel-salt density, the mechanisms by which the SCR responds to such density changes should be investigated.

The analysis considers only the effect of temperature variation, assuming a uniform temperature distribution within the reactor core. Owing to the thermal expansion effect, temperature changes lead to changes in material density. Given the low thermal expansion coefficients and small size of the constituent materials of the SCR, the thermal expansion effect for the SCR is negligible. In contrast, the fuel salt exhibits a high thermal expansion coefficient and significant thermal expansion. Therefore, only the density change of the fuel salt resulting from the temperature variation is considered, whereas the change in the density of the SCR due to temperature variation is neglected. Within a temperature range from a maximum outlet temperature of 750 °C to a cold shutdown temperature of 550 °C, the fuel-salt density changes from about 2665 to 2755 kg/m^3 [55]. If the SCR average density is below 2755 kg/m^3, after a cold shutdown, the resulting decrease in temperature may cause the SCR to float upward, thus posing a risk of reactor recriticality. Thus, the SCR average density should be maintained at above 2755 kg/m^3 to avoid such scenarios. When only the effects of online fueling and reprocessing are considered, the fuel-salt density is expected to increase to approximately 2800 kg/m^3 over the lifetime of the fuel, as heavy metals accumulate in the molten salt [44]. Thus, an SCR with a ρ_s of 2805 kg/m^3 is selected, with the other parameters identical to those

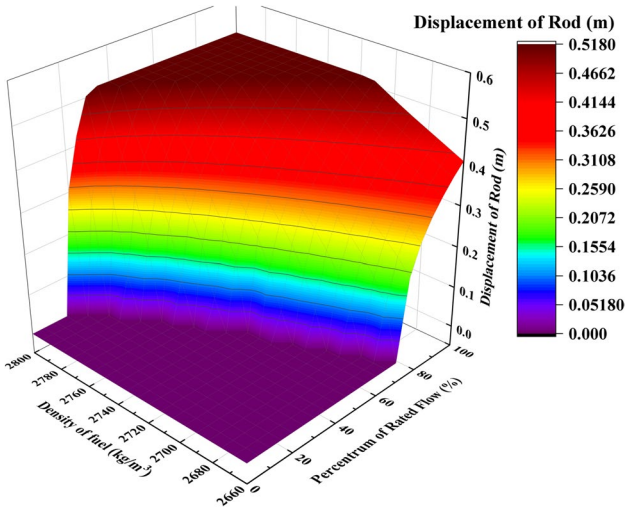

Fig. 9 (Color online) SCR position height correlation with core flow rate and fuel-salt density

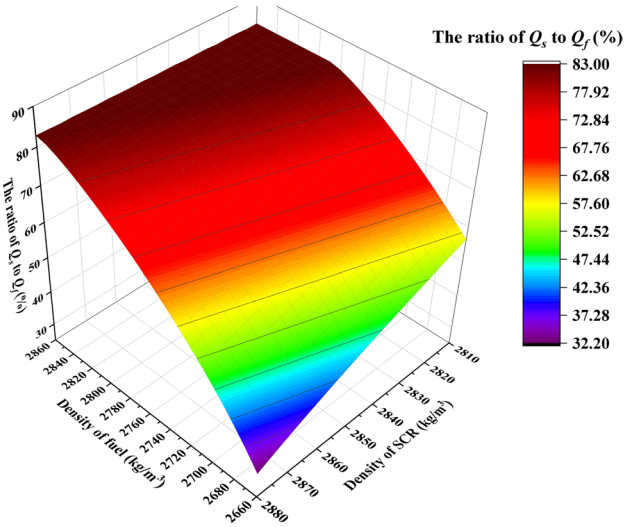

Fig. 10 (Color online) SCR-to-fuel salt channel flow rate ratio correlation with SCR mean density and fuel density

in the previous section, to study the effect of changes in the fuel-salt density on the SCR. The calculations reveal the SCR rod position heights under varying fuel-salt densities and core flow conditions, as illustrated in Fig. 9.

The results show that a decrease in the fuel-salt density elevates the SCR start-up flow threshold while simultaneously reducing its position height at the rated core flow. In other words, an increase in temperature—which leads to a lower density—results in a lower SCR rod position height, thereby introducing a negative reactivity and enhancing the negative temperature reactivity coefficient of the reactor. Furthermore, increasing the fuel-salt density does not change the rod position height at the rated flow because the SCR is already at its uppermost position, restrained at top of the channel. However, higher fuel-salt densities alter the SCR's response under flow-loss conditions, causing it to respond more slowly. When the fuel-salt density is 2800 kg/m^3, the SCR only begins to descend when the core flow decreases to approximately 50% of the rated value. Accordingly, to improve the SCR's resilience against disturbances due to density variations, its average density must be further increased.

Based on conservative estimates that incorporate temperature fluctuations and the effects of online fueling and reprocessing on fuel lifetime, the SCR average density must be maintained above 2855 kg/m^3 under cold conditions at the end of fuel life to prevent the fuel-salt density from surpassing the SCR average density. However, if the SCR average density is extremely high, the pressure drop necessary to drive the SCR increases, which reduces the channel flow and adversely affects the heat transfer performance of the SCR channel. As shown in Fig. 10, if the SCR average density exceeds 2855 kg/m^3 and the fuel-salt density remains at a nominal value of 2710 kg/m^3, the channel flow drops to less than 60% of the fuel channel flow, which is unacceptable for heat transfer safety. However, as the fuel-salt density increases, the average core pressure drop increases, resulting in a greater allocation of the flow to the SCR channel. This, in turn, improves the heat transfer capacity. Thus, as heavy metals accumulate in the molten salt and the fuel-salt density increases, the heat transfer capacity within the SCR channel is enhanced.

In summary, the influence of fuel-salt density variations on the SCR fundamentally depends on the difference between the SCR average and fuel-salt densities. A larger difference enhances the SCR's resistance to density disturbances. However, this may also reduce the heat transfer performance of the channels. Therefore, an optimal balance should be obtained between the SCR's ability to withstand density variations and its heat transfer capability.

4.4 SCR reactivity worth

Because the fluid-driven control and graphite components are integrated within the reactor core, their dimensions are limited by the specifications of the graphite components. Consequently, assessing whether the SCR can satisfy the reactivity control requirements, given these dimensional limitations, is vital. Because the SCR remains entirely within the active region of the core throughout its motion, its reactivity worth is predominantly determined by the neutron flux distribution within the core. Specifically, the larger the neutron flux gradient encountered within the SCR's range of motion, the more significant the change in its reactivity worth, resulting in a higher amount of reactivity

compensation. Because the variations in the upper base diameter, conical taper angle, and average density of the SCR are restricted to narrow ranges and exert minimal influence on its reactivity worth, this paper primarily focuses on analyzing the effects of SCR length, number of units, and spatial placement on reactivity, whereas the effects of the upper base diameter, conical taper angle, and average density are incorporated into the final iterative calculations.

The SCR is designed with a length range of 20–40 cm and deployment quantity of 1–3 units, employing a centrally symmetric arrangement. When deploying three SCR units, a tripartite symmetric arrangement—positioned at the midpoints of the three sides (as indicated by "*" in Fig. 1)—is used. For two SCR units, a bilateral symmetric arrangement at the midpoints is adopted; for a single unit, the midpoint of one side is selected. Using the core central axis (designated as the zeroth ring) as reference, the placement extends outward to the positions of the graphite components in the second, fourth, and sixth rings, as shown in Fig. 1. The core's axial midplane is defined as the reference plane (0 position) for the SCR's height. When calculating the reactivity worth of the SCR, the upper base diameter is fixed at 6 cm, the conical taper angle at 2°, and the average density at 2800 kg/m^3 to ensure an adequate range of motion.

Two SCR units with lengths of 20, 25, 30, 35, and 40 cm, respectively, are deployed at the graphite components in the fourth ring. The reactivity introduced from their lowest to highest positions is computed, and the results are presented in Fig. 11. As the SCR length increases, the reactivity induced by movement exhibits an increasing trend, with the most significant reactivity introduced during the mid-range of motion and lower reactivity in the initial and final phases. Hence, to align with the DNPs flow reactivity–core flow curve shown in Fig. 6, we should configure the SCR's range of motion in the mid-to-rear section. Among all the SCR lengths evaluated, only the 20-cm variant fails to satisfy the 275 pcm reactivity control requirement. To minimize any detrimental effects on neutron economy under normal operating conditions, the SCR length should be reduced as much as possible while still satisfying the reactivity control requirements.

SCRs with a length of 30 cm are deployed in varying quantities and at different locations within the core, and the induced reactivity changes at different heights are computed. The results are presented in Fig. 12. The results indicate that a minimum of two SCR units must be deployed to satisfy the 275-pcm reactivity control requirement. At equal deployment quantities, the reactivity change in the fourth ring exceeds that in the second ring owing to the higher axial neutron flux gradient in the fourth ring. In the sixth ring, with a reduced neutron flux distribution, the reactivity change for the same SCR movement is minimal.

Under normal operating conditions, the SCR is positioned at the top of the active region of the core, in contact with the upper support plate. The corresponding reactivity values for different deployment quantities and positions are summarized in Table 5. The analysis reveals that, for identical deployment quantities, the placement position has a relatively minor impact on the reactivity, with a difference of approximately 60 pcm between the second and sixth rings. However, for an identical deployment position, the number of SCR units significantly affects the reactivity, with three SCRs exhibiting approximately 100 pcm higher reactivity than that with two SCRs.

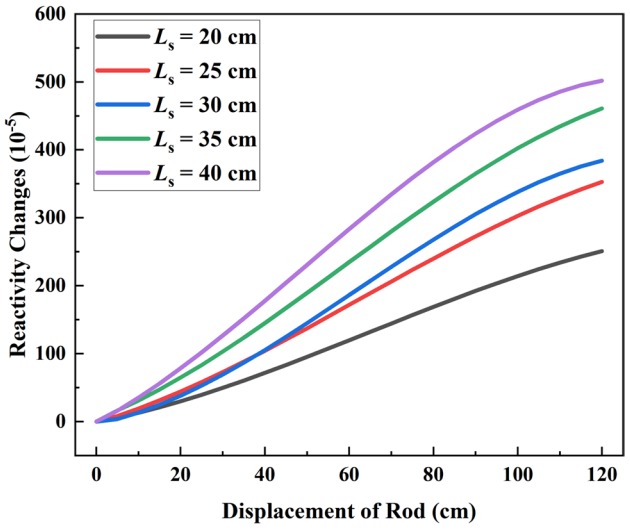

Fig. 11 (Color online) Reactivity changes of SCRs with different lengths at different rod positions (two SCRs at the fourth ring component position)

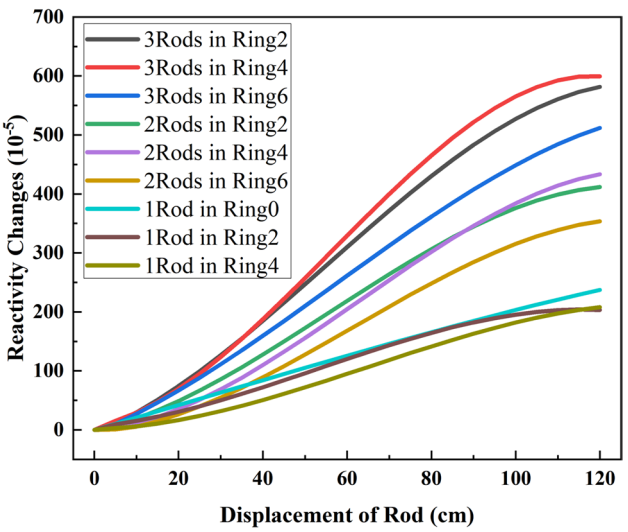

Fig. 12 (Color online) Reactivity changes at different rod positions with different SCR deployment quantities and positions (L_s = 30 cm)

Table 5 SCR neutron absorption reactivity at its highest position

Deployment configuration	Neutron absorption reactivity ($\times 10^{-5}$)
3 Rods in Ring 2 (3R2)	248
3 Rods in Ring 4 (3R4)	223
3 Rods in Ring 6 (3R6)	194
2 Rods in Ring 2 (2R2)	169
2 Rods in Ring 4 (2R4)	109
2 Rods in Ring 6 (2R6)	100

Therefore, the primary focus should be on determining the number of SCR units to be deployed, after which the optimal placement can be refined. For minimal adverse effects of SCR deployment on the neutron economy, core flow distribution, and system compatibility under normal operating conditions, the number of SCR units should be minimized, and their placement should be as far from the core's central axis as possible. Thus, from a purely reactive perspective, deploying two SCR units in the fourth ring is the optimal solution. Under normal operating conditions, the variations in reactivity owing to changes in SCR deployment position and quantity are limited, with a maximum difference of only 148 pcm. Thus, by integrating the SCR rod position–core flow relationship, an optimal deployment scheme can be determined.

4.5 Correlation between SCR reactivity introduction and core flow rate

Based on the preceding analysis, the SCR average density significantly affects the start-up flow threshold, channel flow, and its resistance to density disturbances, whereas the conical taper angle profoundly influences the relationship between the SCR rod position and core flow. In contrast, the SCR length and inlet diameter exert relatively minor impacts on SCR performance. Therefore, this paper omits the effects of SCR length and upper base diameter—fixed at $L_s = 30$ cm and $D_s = 7$ cm—and, according to the procedure shown in Fig. 5, calculates and screens the conical taper angles that satisfy the reactivity compensation criteria. Subsequently, we analyze the reactivity compensation capabilities at different SCR average densities.

With increasing SCR average density, its displacement at rated flow decreases. Hence, a higher SCR average density necessitates larger reactivity insertion. As illustrated in Fig. 7a, when ρ_s is 2840, 2800, and 2760 kg/m^3, the displacements at rated flow are approximately 35, 40, and 50 cm, respectively. According to Fig. 12, to satisfy the reactivity control requirements, the three average density conditions correspond to the following SCR deployment schemes: Three SCR units in the fourth ring for $\rho_s = 2840$ kg/m^3, two SCR units at the fourth ring for $\rho_s = 2800$ kg/m^3, and two SCR units in the 6th ring for $\rho_s = 2760$ kg/m^3. Figure 13 shows the reactivity variations induced by SCR motion across various core flow conditions for these scenarios.

The results reveal that a lower SCR average density produces a more pronounced reactivity compensation over a broader range of core flow variations, whereas a higher SCR average density enables a more rapid response to flow changes. For instance, at $\rho_s = 2760$ kg/m^3, the flow reactivity fluctuations can be confined within 30 pcm over 55%–100% of the rated core flow, but the SCR only introduces −275 pcm of reactivity when the core flow falls below 40% of its rated value. In contrast, at $\rho_s = 2840$ kg/m^3, the flow reactivity fluctuations are suppressed within 30 pcm only in the 80%–100% rated flow range, and −275 pcm reactivity is achieved only when the core flow drops below 68% of the rated value. As shown in Table 6, from the perspective of the neutron economy, the impact differences among these schemes are minimal, with a maximum variance of only 22 pcm. In terms of heat transfer performance, an SCR with

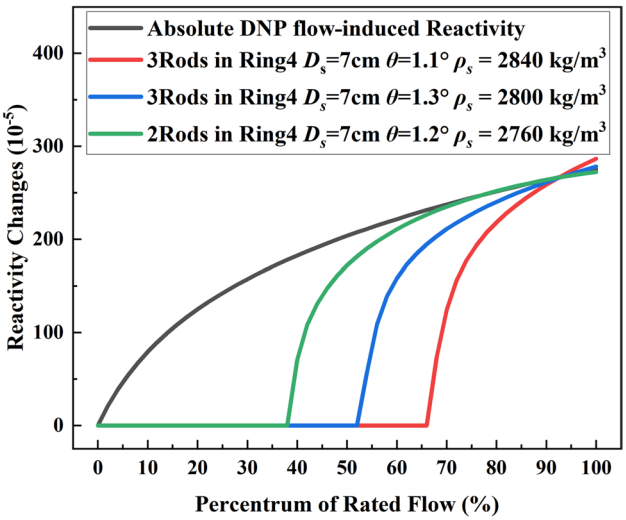

Fig. 13 (Color online) Reactivity introduced by different parameter SCR under various core flow rates

Table 6 SCR channel flow rate and neutron absorption reactivity at maximum elevation

SCR mean density (kg/m^3)	SCR-to-Fuel channel flow rate ratio (%)	Neutron absorption reactivity ($\times 10^{-5}$)
2840	61.46	52
2800	71.43	47
2760	78.67	30

$\rho_s = 2840$ kg/m^3 exhibits a channel flow that amounts to only 61.46% of the fuel channel flow, potentially compromising the heat transfer safety of channels.

In summary, for improved matching between flow and reactivity changes, an SCR with a lower average density should be selected. In contrast, if the response speed of the SCR under loss-of-flow scenarios is of higher priority, a higher average density SCR should be selected. However, note that increasing the average density of the SCR decreases the flow within its channels. Variations in the primary loop flow are generally minimal during MSR operation. However, under accident conditions, the response speed of the SCR is a crucial factor; thus, prioritizing an SCR with a higher average density is more appropriate. Therefore, considering both the response speed and heat transfer safety, the SCR with an average density of $\rho_s = 2800$ kg/m^3 demonstrated a superior performance. However, attention should be paid to the increase in fuel density toward the end of the fuel cycle and under cold-reactor conditions. The average SCR density, timely separation of heavy metals from the fuel is required.

5 Summary

This paper addresses the reactivity variations in molten salt reactors induced by fuel flow by proposing an innovative passive fluid-driven suspended control rod (SCR) design and performing an in-depth feasibility assessment. By developing a mathematical model and conducting sensitivity analysis, we draw the following key conclusions: The SCR passively adjusts its position to dynamically compensate for reactivity changes caused by the fuel flow. Under a defined range of core flow conditions, the SCR is capable of precise reactivity regulation and, during flow loss, introduces negative reactivity, effectively mitigating the positive reactivity excursions resulting from the retention of delayed neutron precursors.

The investigation revealed that the average density and conical taper angle of the SCR are critical parameters that influence the overall performance. The average density significantly affects the start-up flow threshold, response speed, and ability to withstand fuel density variations, whereas the conical taper angle dictates the relationship between the rod position and core flow. The optimization of these two parameters can markedly improve the SCR's responsiveness and its capacity for reactivity compensation.

Furthermore, the its length, deployment quantity, and spatial positioning directly affect both the reactivity compensation effectiveness and the neutron economy. Although longer SCRs and an increased number of units yield enhanced reactivity compensation, they may also adversely affect the core neutron economy. Consequently, SCR design must balance between satisfying the reactivity compensation requirements while minimizing its impact on the neutron economy and core flow distribution.

Featuring a passive driving mechanism, the SCR efficiently compensates for reactivity fluctuations induced by the fuel flow in MSRs. This significantly enhances the inherent safety and operational stability of the reactor. This innovative approach to passive reactivity control has considerable potential for a wide range of applications. Finally, this paper establishes a theoretical basis for the design and optimization of SCRs while offering valuable insights for improving the safety of MSRs.

This study aimed to demonstrate the potential of SCR as an innovative solution for passive reactivity control in MSRs and assess the feasibility of compensating for DNP flow reactivity effects. Note that the current analytical model adopts certain simplifications. Future research will construct a three-dimensional transient multiphysics model to evaluate the dynamic response characteristics quantitatively and the spatial effects of the SCR under complex scenarios, such as abrupt flow transients and power oscillations. Additionally, the long-term service behavior of the SCR under extreme operating conditions should be investigated. In addition, a hydraulic test rig will be developed to validate the accuracy of the theoretical model and refine the empirical coefficients. Future research will focus on a closed-loop strategy that integrates multi-scale mechanistic modeling, experimental validation, and standardized design to drive the SCR from conceptual innovation to engineering application, providing key technical support for enhancing the safety and economic competitiveness of Generation IV molten salt reactors.

Author contributions All authors contributed to the study conception and design. Material preparation, data collection, and analysis were performed by J-TC, G-FZ, and C-QY. The first draft of the manuscript was written by J-TC and all authors commented on previous versions of the manuscript. All authors read and approved the final manuscript.

Data availability The data that support the findings of this study are openly available in Science Data Bank at https://cstr.cn/31253.11.sciencedb.j00186.00775 and https://doi.org/10.57760/sciencedb.j00186.00775.

Declarations

Conflict of interest The authors declare that they have no conflict of interest.

References

1. B. Mignacca, G. Locatelli, Economics and finance of MSRs. Prog. Nucl. Energy **129**, 103503 (2020). https://doi.org/10.1016/j.pnucene.2020.103503
2. L.Y. He, Y. Cui, L. Chen et al., Effect of reprocessing on neutrons of a molten chloride salt fast reactor. Nucl. Sci. Tech. **34**, 46 (2023). https://doi.org/10.1007/s41365-023-01186-3

3. D. Zhang, L. Liu, M. Liu et al., Review of conceptual design and fundamental research of molten salt reactors in China. Int. J. Energy Res. **42**, 1834–1848 (2018). https://doi.org/10.1002/er.3979
4. J. Serp, M. Allibert, O. Beneš et al., The molten salt reactor (MSR) in generation IV: overview and perspectives. Prog. Nucl. Energy **77**, 308–319 (2014). https://doi.org/10.1016/j.pnucene.2014.02.014
5. X.D. Zuo, M.S. Cheng, Y.Q. Dai et al., Flow field effect of delayed neutron precursors in liquid-fueled molten salt reactors. Nucl. Sci. Tech. **33**, 96 (2022). https://doi.org/10.1007/s41365-022-01084-0
6. T.G. Xui, Study of a one hundred megawatt liquid MSR loss of flow ATWS accidents and control rod withdrawal ATWS accidents. Dissertarion, Shanghai Institute of Applied Physics, Chinese Academy of Sciences, 2022. https://doi.org/10.27585/d.cnki.gkshs.2022.000078
7. J. Cai, X.B. Xia, K. Chen et al., Analysis on reacivity initiated transient from control rod failure events of a molten salt reactor. Nucl. Sci. Tech. **25**, 030602 (2014). https://doi.org/10.13538/j.1001-8042/nst.25.030602
8. J. Xie, T. Hui, Y. Liu et al., Neutronic design and dynamic analysis of a 450 MWth graphite molten salt reactor core. Ann. Nucl. Energy **152**, 107984 (2021). https://doi.org/10.1016/j.anucene.2020.107984
9. I. Pioro, Handbook of generation-IV nuclear reactors. ASME J. Nucl. Rad. Sci. **3**, 026501 (2017). https://doi.org/10.1115/1.4035327
10. S. Nakanishi, T. Hosoya, S. Kubo et al., Development of passive shutdown system for SFR. Nucl. Tech. **170**, 181–188 (2010). https://doi.org/10.13182/NT10-A9456
11. A. Nayak, R. Sinha, Role of passive systems in advanced reactors. Prog. Nucl. Energy **49**, 486–498 (2007). https://doi.org/10.1016/j.pnucene.2007.07.007
12. Z.J. Yang, J.L. Gou, J.L. Gou et al., Analysis of SBLOCA on CPR1000 with a passive system. Nucl. Sci. Tech. **28**, 10 (2017). https://doi.org/10.1007/s41365-016-0154-y
13. Y.K. Buksha, Y.E. Bagdassarov, A.I. Kiryushin et al., Operation experience of the BN-600 fast reactor. Nucl. Eng. Des. **173**, 67–79 (1997). https://doi.org/10.1016/S0029-5493(97)00097-6
14. V.M. Poplavskii, A.N. Chebeskov, V.I. Matveev, BN-800 as a new stage in the development of fast sodium-cooled reactors. At. Energy **96**, 386–390 (2004). https://doi.org/10.1023/B:ATEN.0000041204.70134.20
15. W.J. Hu, L.X. Ren, Z.X. Li et al., Study on technical scheme for passive shutdown of pool-type sodium-cooled fast reactor. Nucl. Sci. Eng. **34**, 23–27 (2014)
16. Y.Y. Zhang, T.Y. Duan, S.M. Chen et al., Research and design of control system of liquid suspended passive control rod. Instrumentation **27**, 64–67 (2020). https://doi.org/10.3969/j.issn.1002-1841.2020.05.011
17. B.X. Hu, Y.W. Wu, W.X. Tian et al., Development of a transient thermal-hydraulic code for analysis of China Demonstration Fast Reactor. Ann. Nucl. Energy **55**, 302–311 (2013). https://doi.org/10.1016/j.anucene.2012.12.022
18. J. Song, Y. Wu, W. Tian, et al., Characterization and experimental investigation for the dynamic performance of the hydraulically suspended passive shutdown system in China sodium-cooled fast reactor, in *26th International Conference on Nuclear Engineering*, England, 22–26 July 2018. https://doi.org/10.1115/ICONE26-81294
19. X. Wang, B. Kuang, P. Liu et al., Performance test of conceptually designed hydraulically suspended passive shut down subassembly for CFR600. Prog. Nucl. Energy **140**, 103906 (2021). https://doi.org/10.1016/j.pnucene.2021.103906
20. Y. Ren, H. Yu, Conjugate heat transfer numerical analysis of guide tube of sodium-cooled fast reactor hydraulic suspended passive shutdown mechanism. At. Energy Sci. Tech. **54**, 615–623 (2020). https://doi.org/10.7538/yzk.2019.youxian.0316
21. X.Y. Yang, M.Z. Wang, H. Yan et al., The research of technology readiness assessment of hydraulic suspended passive shutdown system. Sci. Tech. Vis. **2018**, 6–8 (2018). https://doi.org/10.19694/j.cnki.issn2095-2457.2018.16.003
22. Y. Li, Development and verification of the thermal-hydraulic design program for the passive shutdown assembly. Nucl. Sci. Eng. **41**, 378–385 (2021). https://doi.org/10.11889/j.0253-3219.2021.hjs.41.020378
23. X. Wang, B. Kuang, P. Liu et al., Dynamic performance investigation on the hydraulic-suspended passive shutdown subassembly of SFR. Ann. Nucl. Energy **158**, 108244 (2021). https://doi.org/10.1016/j.anucene.2021.108244
24. B. Kuang, X. Wang, J. Hou et al., Studying dynamical and hydraulic characteristics of the hydraulically suspended passive shutdown subassembly (HS-PSS) and validating with a prototypic test sample. Energies **17**, 5038 (2024). https://doi.org/10.3390/en17205038
25. X. Wang, B. Kuang, P. Liu et al., Performance study of moving body dynamics in hydraulic suspended PSS for SFR under unprotected loss of flow accident. At. Energy Sci. Tech. **52**, 920–925 (2018). https://doi.org/10.7538/yzk.2018.52.05.0920
26. H. Yuan, Hydraulic characteristics analysis and experimental verification of hydraulically suspended passive shutdown subassembly. Dissertation, Shanghai Jiao Tong University, 2019. https://doi.org/10.27307/d.cnki.gsjtu.2019.004274
27. G. Peng, Development of hydraulic design code for fast reactor hydraulically suspended passive shutdown subassembly. Dissertation, Shanghai Jiao Tong University, 2018. https://doi.org/10.27307/d.cnki.gsjtu.2018.004916
28. Z. Yang, S. Shi, B. Wei et al., Experimental and numerical study on the critical working condition of control rod in liquid-suspended shutdown device. Ann. Nucl. Energy **159**, 108304 (2021). https://doi.org/10.1016/j.anucene.2021.108304
29. H. Wang, Y. Liu, D. Lu et al., Experimental and numerical research on flow-induced vibration characteristics of hydraulic suspended passive shutdown subassembly in SFR. Prog. Nucl. Energy **170**, 105131 (2024). https://doi.org/10.1016/j.pnucene.2022.105131
30. Z. Yang, S. Shi, Q. Zhang et al., Research and optimization design of buffer protection in passive shutdown subassemblies. Prog. Nucl. Energy **139**, 103875 (2021). https://doi.org/10.1016/j.pnucene.2021.103875
31. G. Li, D. Cai, S. Li et al., The influence of groove structure parameters on the maximum flow resistance of a rectangular narrow channel. Energies **13**, 3716 (2020). https://doi.org/10.3390/en13143716
32. Y. Liu, Study on characteristics of liquid suspension passive structure and buffer segment optimization. Dissertation, Xi'an University of Technology, 2019. https://doi.org/10.27398/d.cnki.gxalu.2019.000072
33. B. Xue, Experimental study on the control rod motion characteristics of hydraulic suspended passive components. Dissertation, Xi'an University of Technology, 2019. https://doi.org/10.27398/d.cnki.gxalu.2019.000296
34. M. Hao, Analysis of falling characteristics and abnormal station suspension state of liquid suspended passive shutdown components. Dissertation, Xi'an University of Technology, 2020. https://doi.org/10.27398/d.cnki.gxalu.2020.001626
35. E.D. Blandford, P.F. Peterson, A buoyantly-driven shutdown rod concept for passive reactivity control of a fluoride salt-cooled high-temperature reactor. Nucl. Eng. Des. **262**, 600–610 (2013). https://doi.org/10.1016/j.nucengdes.2013.05.025
36. C. Kim, Y. Kim, FAST (Floating Absorber for Safety at Transient) for the improved safety of metallic-fuel-loaded sodium-cooled fast

reactors. Trans. Am. Nucl. Soc. **121**, 1545–1548 (2019). https://doi.org/10.13182/T31261
37. M.J. Delaney, G.E. Apostolakis, M.J. Driscoll, Risk-informed design guidance for future reactor systems. Nucl. Eng. Des. **235**, 1537–1556 (2005). https://doi.org/10.1016/j.nucengdes.2005.01.004
38. C. Kim, Y. Kim, Potential of FAST (floating absorber for safety at transient) as a solution for positive coolant temperature coefficient in sodium-cooled FAST reactors. Ann. Nucl. Energy **137**, 107048 (2020). https://doi.org/10.1016/j.anucene.2019.107048
39. C. Kim, S. Jang, Y. Kim, FAST (floating absorber for safety at transient) for the improved safety of sodium-cooled burner fast reactors. Nucl. Eng. Tech. **53**, 1747–1755 (2021). https://doi.org/10.1016/j.net.2020.12.004
40. S. Lee, Y.H. Jeong, Performance evaluation of the floating absorber for safety at transient (FAST) in the innovative sodium-cooled fast reactor (iSFR) under a single control rod withdrawal accident. Nucl. Eng. Tech. **52**, 1110–1119 (2020). https://doi.org/10.1016/j.net.2019.11.011
41. A.A.E. Abdelhameed, C. Kim, Y. Kim, Improved FAST device for inherent safety of oxide-fueled sodium-cooled fast reactors. Energies **14**, 4610 (2021). https://doi.org/10.3390/en14154610
42. S. Lee, Y. Kim, Y. Choi et al., A study of the behavior of the floating absorber for safety at transient (FAST) in an innovative sodium-cooled fast reactor (iSFR). Ann. Nucl. Energy **179**, 109364 (2022). https://doi.org/10.1016/j.anucene.2022.109364
43. S. Lee, Y.H. Jeong, Inherent safety enhancement by design optimization of a floating absorber for safety at transient (FAST) in an advanced burner reactor. Ann. Nucl. Energy **172**, 109026 (2022). https://doi.org/10.1016/j.anucene.2022.109026
44. G.F. Zhu, X.Z. Kang, C. Zou, Design reference scheme of 150 MW thorium-based molten salt demonstration reactor. Dissertation, Shanghai Institute of Applied Physics, Chinese Academy of Sciences, 2018
45. S. Bakhri, Investigation of rod control system reliability of PWR reactors. KnE. Energy **1**, 94–105 (2016). https://doi.org/10.18502/ken.v1i1.465
46. G.M. Tolson, A. Taboada, *MSRE Control Elements: Manufacture, Inspection, Drawings, and Specifications* (Oak Ridge National Lab. (ORNL), Oak Ridge, TN, 1967)
47. S.H. Yu, Y.F. Liu, P. Yang et al., Effect analysis of core structure changes on reactivity in molten salt experimental reactor. Nucl. Tech. **42**, 82–86 (2019). https://doi.org/10.11889/j.0253-3219.2019.hjs.42.020603
48. P.K. Romano, B. Forget, The OpenMC Monte Carlo particle transport code. Ann. Nucl. Energy **51**, 274–281 (2013). https://doi.org/10.1016/j.anucene.2012.06.040
49. G.F. Zhu, R. Yan, H.H. Peng et al., Application of Monte Carlo method to calculate the effective delayed neutron fraction in molten salt reactor. Nucl. Sci. Tech. **30**, 34 (2019). https://doi.org/10.1007/s41365-019-0557-7
50. P. Haubenreich, J. Engel, B. Prince, et al., MSRE design and operations report. Part III. Nuclear analysis. Oak Ridge National Laboratory Report (1964). https://doi.org/10.2172/4114686
51. I.E. Idelchik, M. Steinberg, O.G. Martynenko, *Handbook of Hydraulic Resistance* (Hemisphere Publishing Corporation, New York, 1986)
52. I. Suvorova, Investigating the hydrodynamics of flows in channels of complex geometric forms, in *International Conference on Differential Equations, Mathematical Physics and Applications*, 2017
53. I. Idelchik, *Flow Resistance: A Design Guide for Engineers* (Routledge, London, 2017). https://doi.org/10.1201/9780203755754
54. S.S. Zolotov, *Hydraulic Resistance of Channels of Annular Cross Section* (Proceedings from the Leningrad Ship-building Institute, 1971), pp. 41–49
55. G.F. Zhu, Y. Zou, R. Yan, et al., Volume change analysis of primary loop in a small modular thorium-based MSR, in *29th International Conference on Nuclear Engineering*, 8–12 August 2022. https://doi.org/10.1115/ICONE29-90295